Analysis of coupled axial and lateral deformation of roots in soil

Meijer, Gerrit J.; Muir Wood, David; Knappett, Jonathan; Bengough, Anthony; Liang, Teng

Published in:
International Journal for Numerical and Analytical Methods in Geomechanics

DOI:
10.1002/nag.2880

Publication date:
2019

Received: 18 April 2018 | Revised: 25 October 2018 | Accepted: 26 October 2018

DOI: 10.1002/nag.2880

RESEARCH ARTICLE

WILEY

Analysis of coupled axial and lateral deformation of roots in soil

Gerrit J. Meijer[1] | David Muir Wood[1] | Jonathan A. Knappett[1] | Glyn A. Bengough[1,2] | Teng Liang[1]

[1]School of Science and Engineering, University of Dundee, Dundee, UK

[2]James Hutton Institute, Dundee, UK

Correspondence
Gerrit J. Meijer, School of Science and Engineering, University of Dundee, Dundee DD1 4HN, UK.
Email: g.j.z.meijer@dundee.ac.uk

Funding information
EPSRC, Grant/Award Number: EP/M020355/1

Summary

Plant roots can help to stabilise slopes. Existing analytical models to predict their mechanical contribution are however limited: they typically focus on the ultimate limit state, employ various empirical factors, and ignore much of the underlying root-soil interaction. A new model was developed based on large deflection Euler-Bernoulli elastic beam theory that can be used to study the mobilisation of root strength under various loading conditions (direct shear and pull-out). Both lateral and axial loading of the root by the soil were incorporated, based on existing methodologies for foundation piles (p-y and t-z curves). The model is able to take the key parameters into account (root biomechanical properties, root architectural properties, and soil properties) while remaining quick to solve using a numerical boundary value problem solver. The model was compared with experimental direct shear test data using various root analogues (rubber, plastic, and wood) in dry sand with various densities and effective stress levels and was able to accurately predict the measured shear force-displacement behaviour. Comparison with experimentally measured pull-out force-displacement curves using rubber and wooden root analogues with various architectures in dry and partially saturated sands was also satisfactory. In the future, this model can aid with addressing long-standing problems in the root-reinforcement community: quantifying the effect of (sequential) mobilisation of root strength in direct shear, the effect of the angle at which the root crosses a shear plane, the effect of root topology on root-reinforcement or the effect of root bending, and root shear shear forces on root-reinforcement.

KEYWORDS

direct shear, Euler-Bernoulli beam, pull-out, reinforcement, roots, soil

1 | INTRODUCTION

The mechanical action of roots can help to reinforce slopes against deformation and failure. Roots can provide additional hydromechanical reinforcement by enhancing soil matric suction through water uptake. However, their contribution is

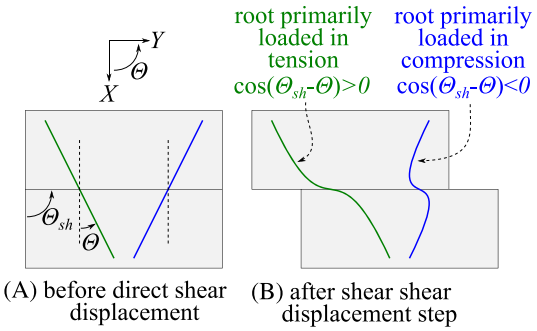

FIGURE 1 Schematic representation of roots loaded in direct shear [Colour figure can be viewed at wileyonlinelibrary.com]

difficult to quantify due to the complicated nature of the interaction between the root systems and the soil. The magnitude of mechanical reinforcement depends on root properties (eg, strength, stiffness, and cross-sectional shape), soil properties (eg, stress-strain behaviour), root-soil interaction properties (eg root-soil friction), and root architectural properties (eg, root tortuosity, angle between root and shear plane, root branching and connectivity), all of which might vary in time and space.

Various models to quantify mechanical root reinforcement have been developed, with various amounts of simplification. The most well-known root-reinforcement model expresses the ultimate contribution of a single root to shear resistance as an increase in the apparent cohesion of the rooted soil (c_r, dubbed "root cohesion"), after Wu et al[1] (WWM):

$$c_r = k' \sigma_t \frac{A}{A_{sh}}, \tag{1}$$

where σ_t is the root tensile strength, A is the cross-sectional area of an individual root, and A_{sh} is the cross-sectional area of the shear plane. To find the total reinforcement, the contributions of all individual roots are summed. k' is a coefficient based on the angle of the root (Θ) and the direction of shearing (Θ_{sh}; see Figure 1):

$$k' = \cos(\Theta_{sh} - \Theta) + \sin(\Theta_{sh} - \Theta) \tan \phi', \tag{2}$$

where ϕ' is the angle of internal friction of the soil. The first term in this equation reflects the influence of the component of the tensile force in the fibre in the direction of shearing. The second term indicates the component normal to the shear plane, causing an increase in normal stress on the shear plane. Often, $k' = 1.2$ is assumed.[1] By superimposing the effect of each individual root, the total reinforcement can be obtained.

This approach has some severe drawbacks:

1. The root is assumed to be loaded in pure tension, and this analysis is therefore only valid for "thin" roots with low bending stiffness. Although the literature has recognised that "thicker" roots will be loaded in bending/shear, the threshold between "thin" and "thick" has never been quantified in terms of root properties such as diameter and stiffness. The contribution of roots with diameters exceeding 10 mm is generally ignored, arguing that their numbers are low and that they have low tensile strength compared with thin roots. Simplification by ignoring thick roots has however never been justified in a quantitative way.
2. The model cannot deal with roots loaded in compression ($\cos(\Theta_{sh} - \Theta) < 0$; see Figure 1). An analytical attempt has been made to predict the root-reinforcement for soils loaded in compression by Schwarz et al[2] but only for roots loaded in pure compression. These authors used a highly simplified model, fitting the relationship between root diameter and buckling resistance using a two-parameter power law with empirically determined coefficients.
3. It is assumed that all roots mobilise strength simultaneously. However, in reality, some might have broken already before others are mobilised because of differences in, for example, root strength, stiffness, or orientation. Thus, the WWM model will overestimate the root-reinforcement. Fibre bundle models (FBM) have been proposed by various authors to account for sequential tensile root failure (eg, Pollen and Simon[3]), adopting a load sharing algorithm based on root diameter. This approach yields an additional reduction factor that can be used in Equation 1. However, the magnitude of this factor strongly depends on the load sharing rules adopted (eg, Mao et al[4]), and load sharing rules are generally not based on the actual physical loading mechanism. Also, current FBM suffer from drawbacks (1) and (2) above.

4. The model assumes roots are unbranched, straight features that are not interconnected. To calculate the reinforcement by a bundle of roots, reinforcements by the individual roots are simply superimposed with no potential interconnection or interaction. Thus, the effects of root branching, root architecture, root-soil-root interaction, and root tortuosity are ignored. Root tortuosity results in increased axial anchorage of the root and changes the (apparent) stiffness characteristics during axial pull-out of the root. Real root systems are interconnected networks, and this is likely to have some but currently unknown effect on the root-reinforcement.
5. A finite relative soil-root displacement is required for roots to mobilise reinforcement, which is not considered in the WWM or FBM approach. Therefore c_r can only be used in ultimate limit state geotechnical analyses (eg, stability of a slope but not seasonal deformation response).

Many of these shortcomings can be addressed by using finite element (FE) analysis, using separate root and soil elements (eg, Dupuy et al[5] and Mickovski et al[6]). However, the computational cost of these models makes them unsuitable for large parametric studies or the study of large boundary value problems, where there are many orders of magnitude of size difference between the individual roots and the geotechnical system as a whole. Alternatively, a single constitutive law for the rooted soil can be established, for example, see models for fibre-reinforced sands.[7-9] However, these assume roots behave as one-dimensional tensile elements and also do not directly include branching and architecture effects, making them unsuitable for "thicker" roots where bending and architecture effects might play a role.

A good compromise between the WWM type of models and finite element analyses is the use of Winkler beam-spring-supported models. These have been suggested and applied for roots in the past,[10-12] although the axial loading component was either ignored or set to a constant value, so that an analytical solution could be found for the Euler-Bernoulli differential equation for beam bending:

$$EI\frac{\mathrm{d}^4w}{\mathrm{d}x^4} = q_l + N\frac{\mathrm{d}^2w}{\mathrm{d}x^2}, \tag{3}$$

where EI is the elastic bending stiffness, and w is the transverse displacement along the root axis x. q_l is a transverse loading term, and N is the axial force (assumed constant) in the root. Transverse loading was either linear elastic[10] or constant.[12,13] Duckett[14] and Liang et al[15] used a numerical implementation of such a model in ABAQUS, basing the transverse resistance term q_l on a non-linear model for resistance on laterally loaded piles.[16] Such models maintain the key components that govern the behaviour of the root (root mechanical properties, root architecture/orientation, and soil-root interaction) while minimising computational cost compared with FE analyses. Liang et al[15] further demonstrated that such models can be used to define equivalent continuum properties for use in FE analyses of large boundary value problems, ie, a computationally efficient hybrid approach that can work across multiple scales. However, a drawback of methods based on Equation 3 is that differential equations of this type are only valid for roots undergoing small deflections/deformations. However, in reality, roots can be quite flexible compared with the surrounding soil, which can result in large, localised deflections around the shear plane, as will be shown later in this paper.

In this paper, an extended version of such a beam model is proposed that can be solved without the use of finite element/finite difference software, incorporating the coupled effects of both bending and axial (frictional) loading terms, in a form that is valid for large deformations. This model could therefore be used to provide more representative input information for defining equivalent continuum properties of FE analyses of boundary value problems. The axial and transverse soil-root resistances are based on existing geotechnical methodologies for foundation piles, using *t-z* and *p-y* theory, respectively. The model is validated against laboratory tests of various root analogues (rubber, plastic, and wood) in sands with various densities. Experimental data on root analogues loaded both in direct shear and in axial pull-out were considered in order to validate the model against a wide range of loading conditions.

2 | MODEL DESCRIPTION

2.1 | Governing equations

Various coordinate systems are defined. The global coordinate system (denoted with capitals) is aligned in such a way that the X-axis points down into the soil and the Y-axis denotes the horizontal position, perpendicular to the X-axis. Θ is the (counterclockwise) angle between an axis and the X-axis. The root system consists of multiple straight, interconnected

root segments with initial orientation Θ_0. x and y denote a local coordinate system for an individual root segment, with x aligned along the nondisplaced root axis. θ denotes the angle of a displaced root segment axis with respect to x. s is the coordinate along the deformed root (Figure 2).

The behaviour of a single root segment is modelled using a system of two differential equations. The first one describes the change in axial strain due to root deformation and axial loading (see Appendix A for derivations of the differential equations):

$$-q_a = E_t A \frac{\mathrm{d}\epsilon}{\mathrm{d}s} + E_b I \frac{\mathrm{d}^2\theta}{\mathrm{d}s^2} \frac{\mathrm{d}\theta}{\mathrm{d}s}, \tag{4}$$

where q_a is the root-soil interface friction per unit length of root, E_t and E_b are the elastic root tensile and bending stiffness, A is the root cross-sectional area, I is the second moment of area for the root, and ϵ_a is the axial strain in s-direction.

The second differential equation describes the bending behaviour:

$$E_b I \frac{\mathrm{d}^2\theta}{\mathrm{d}s^3} = q_l + N \frac{\mathrm{d}\theta}{\mathrm{d}s} = q_l + E_t A \epsilon_a \frac{\mathrm{d}\theta}{\mathrm{d}s}, \tag{5}$$

where q_l is the transverse soil resistance per unit root length, and N is the axial force.

To obtain the root displacement in the x and y directions (u and w), two further differential equations have to be solved (Figure 3):

$$\frac{\mathrm{d}u}{\mathrm{d}s} = (1 + \epsilon_a)\cos\theta - 1, \tag{6}$$

$$\frac{\mathrm{d}w}{\mathrm{d}s} = (1 + \epsilon_a)\sin\theta. \tag{7}$$

Because the x-y coordinate system is aligned with the nondisplaced root segment, the displaced root segment positions in x-y space can be described as follows (Figure 2):

$$x = s + u, \tag{8}$$

$$y = w. \tag{9}$$

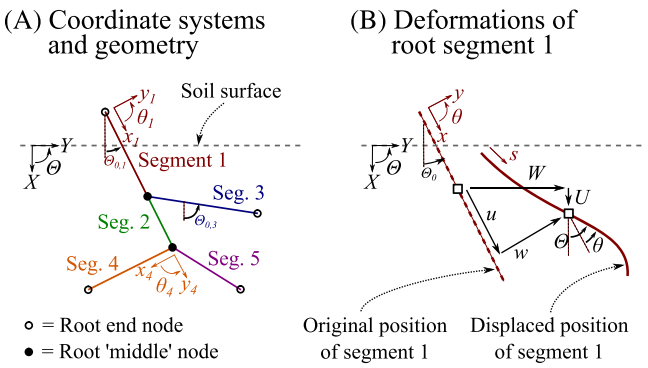

FIGURE 2 Coordinate system and displacement definitions [Colour figure can be viewed at wileyonlinelibrary.com]

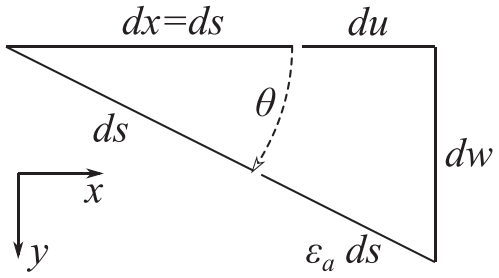

FIGURE 3 Link between root axial strain ϵ_a, segment rotation θ, and root deformations defined in the x-y coordinate system aligned with the nondisplaced root (u and w)

Solving Equations 4-7 simultaneously yields the root segment deformations in all degrees of freedom expressed in terms of the local coordinate system *x-y*. This system of equations requires six boundary conditions to solve. Three conditions can be defined at each end of the root segment (one for every degree of freedom), either in terms of displacements or internal forces. For a formulation for the internal axial force N, shear force V, and bending moment M, see Appendix A.

In writing these equations, it is assumed that q_a and N act parallel to the *deformed* root axis and that q_l and V act perpendicular to this axis. This contrasts with previously used small deformation bending models such as Equation 3, where loads are defined with respect to the original root axis.

2.2 | Soil stress distribution

The magnitude of the soil resistance to relative soil-root displacement depends on the stress level in the soil. The vertical effective stress σ'_v at depth X is defined as

$$\sigma'_v = \sigma'_{v,0} + X\gamma', \tag{10}$$

where $\sigma'_{v,0}$ is the overburden pressure at the soil surface, and γ' is the soil effective unit weight. Some smoothing was applied over a zone $-5 \leq X \leq 5$ mm using hyperbolic tangent sigmoid curves to guarantee a continuously differentiable curve that also ensured $\sigma'_v \approx 0$ when $X < 0$ (points located above the soil surface).

2.3 | Ultimate transverse root-soil resistance

The soil resistance against transverse displacement is modelled based on theory developed for the soil resistance on laterally loaded foundation piles, so called *p-y* theory (eg, Randolph and Gourvenec[17]). Here, the ultimate transverse resistance p_u is calculated using the *p-y* theory for vertical piles in drained fully saturated sand developed by Reese and Van Impe,[16] as used also by Liang et al,[15] though other existing *p-y* formulations for different soils could be used if required. Close to the soil surface, wedge failure might occur, resulting in an ultimate transverse resistance per unit length of root equal to

$$\begin{aligned} p_{st} = \sigma'_v \Bigg[& \frac{K_0 X \tan\phi' \sin\beta}{\tan(\beta-\phi')\cos\alpha} + \frac{\tan\beta}{\tan(\beta-\phi')}\left(d + X\tan\beta\tan\alpha\right) \\ & + K_0 X \tan\beta\left(\tan\phi'\sin\beta - \tan\alpha\right) - K_a d \Bigg], \end{aligned} \tag{11}$$

where K_a and K_0 are coefficients of lateral earth pressure in the active state and at rest, respectively, defined as $K_0 = 0.4$ and $K_a = (1-\sin\phi')/(1+\sin\phi')$. Furthermore, $\alpha = \phi'/2$, $\beta = 45° + \phi'/2$ and ϕ' the soil friction angle. Wedge failure will not occur at larger depth, where the confining stress is greater, and the resistance is calculated as

$$p_{sd} = d\sigma'_v\left[K_a\left(\tan^8\beta - 1\right) + K_0\tan\phi'\tan^4\beta\right]. \tag{12}$$

The maximum soil resistance p_u is given by

$$p_u = \overline{A}_s \min\left(p_{st}, p_{sd}\right), \tag{13}$$

where $\overline{A}_s$ is an empirical multiplication factor for monotonic loading (different values exist for cyclic loading cases), approximated from Figure 3.24 in Reese and Van Impe[16]:

$$\overline{A}_s \approx \begin{cases} 0.88 + 0.0988\left(\frac{X}{d} - 4.5\right)^2 & \frac{X}{d} \leq 4.5 \\ 0.88 & \frac{X}{d} > 4.5 \end{cases}. \tag{14}$$

2.4 | Ultimate axial root-soil resistance

The maximum axial soil-root resistance per unit root surface area (τ_u) is modelled as purely frictional:

$$\tau_u = \sigma'_n \tan\delta, \tag{15}$$

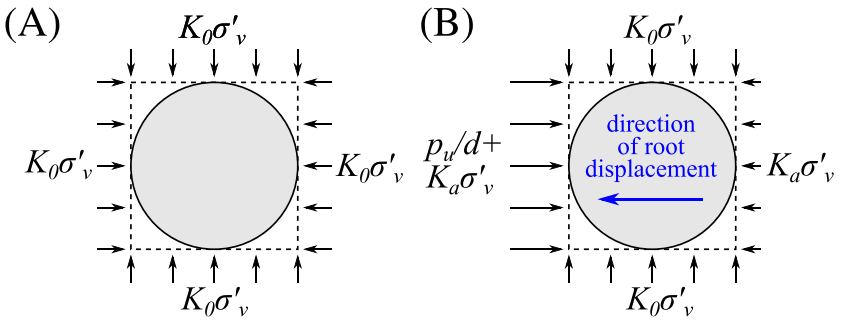

FIGURE 4 Normal stress around the root A, when at rest or B, when laterally displaced [Colour figure can be viewed at wileyonlinelibrary.com]

where σ'_n is the average normal effective stress acting on the soil-root interface, and δ is the soil-root interface friction angle. For a vertical root, the normal stress depends on the horizontal stress as well as an additional contribution due to the the mobilisation of transverse soil resistance:

$$\sigma'_n = K\sigma'_v + \sigma'_{n,l}, \tag{16}$$

where K is the coefficient of lateral earth pressure, and $\sigma'_{n,l}$ is the increase in average normal stress due to transverse root-soil resistance. The underlying assumptions in the p-y model by Reese and Van Impe[16] are that active earth pressure is present behind a laterally displacing pile and that p_u/d is the difference in the pressure ahead of the laterally displacing pile. Assuming an initial normal stress $K_0\sigma'_v$, the increase in normal stress due to a transversely displacing root can be estimated by averaging the change in stress in front, behind, and to the two sides of the pile (see Figure 4):

$$\sigma'_{n,l} \approx \frac{1}{4}\left(\frac{p_u}{d} + K_a\sigma'_v - K_0\sigma'_v\right) + \frac{1}{4}\left(K_a\sigma'_v - K_0\sigma'_v\right) = \frac{1}{2}K_a\sigma'_v - \frac{1}{2}K_0\sigma'_v + \frac{1}{4}\frac{p_u}{d}. \tag{17}$$

2.5 | Mobilisation of soil resistances

Some magnitude of relative displacement between root and soil is necessary in order to fully mobilise either the axial or the transverse resistance. This is modelled using a hyperbolic tangent curve, similar to p-y curves proposed by the American Petroleum Institute.[18] This type of curve has the dual advantage of (1) having an asymptote so that the soil resistance cannot exceed a certain value (p_u or τ_u) and (2) being also valid for negative displacements (ie, for directionality of shear to be considered, which is important as the relative soil-root displacement changes direction when the root crosses the shear plane, or in the case of cyclic loading). The fraction of the maximum axial (ζ_a) and transverse soil resistance that is mobilised (ζ_l) is

$$\zeta_a = \tanh\left(\frac{\Delta u}{b_a}\right), \tag{18}$$

$$\zeta_l = \tanh\left(\frac{\Delta w}{b_l}\right), \tag{19}$$

where Δu and Δw are the relative soil-root displacements in axial and transverse directions, and b_a and b_l are parameters governing the mobilisation distance. The mobilised axial and transverse root-soil resistances can now be defined as

$$q_a = \pi d\zeta_a\left(K\sigma'_v + |\zeta_l|\sigma'_{n,l}\right)\tan\delta, \tag{20}$$

$$q_l = \zeta_l p_u. \tag{21}$$

For dry medium dense sand and dense sand, Reese and Van Impe[16] suggest an initial lateral p-y stiffness of $k_{py} = 24.4X_{eq}$ MNm^{-3} and $k_{py} = 61.0X_{eq}$ MNm^{-3}, respectively, where X_{eq} is the depth. Because these are derived for cases with no overburden pressure, it has been assumed here that $X_{eq} = X + \sigma'_{v,0}/\gamma'$. Here, medium dense is defined as sand with $30° \leq \phi' < 36°$ and dense sand as having $\phi' \geq 36°$. $k_{py}X_{eq}$ should be equal to the initial stiffness of the curve described by Equation 21, therefore,

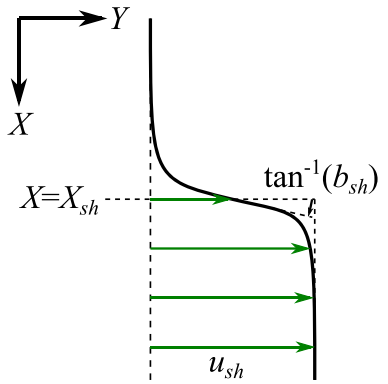

FIGURE 5 Hyperbolic tangent soil displacement curve [Colour figure can be viewed at wileyonlinelibrary.com]

$$b_l = \frac{p_u}{k_{py} X_{eq}}. \tag{22}$$

Combining Equations 21 and 22 gives a much simpler *p-y* curve while maintaining the key elements (initial stiffness and ultimate resistance) compared with the multisegmented methodology suggested by Reese and Van Impe.[16]

The axial mobilisation distance b_a was set to 0.5 mm: this implies that 90% of the axial friction is mobilised after a relative axial soil-root displacement of 0.74 mm. This is based on experimental observation of pull-out resistance of vertical straight 3D-printed acrylonitrile butadiene styrene (ABS) plastic rods in dry sand, in which it was observed that the peak pull-out resistance was mobilised after 0.5 to 1.0 mm displacement and was diameter independent ($1.6 \leq d \leq 12.0$ mm).

Where the soil is able to displace around the roots, as in landslides or a shear box, the soil shear plane is assumed to be parallel to the soil surface. The soil deformation (at any depth X) is modelled using a hyperbolic tangent curve (see Figure 5):

$$U_s = 0, \tag{23}$$

$$W_s = \frac{1}{2} u_{sh} \left(1 + \tanh \left(\frac{X - X_{sh}}{b_{sh}} \right) \right), \tag{24}$$

where U_s and W_s are the soil displacements in the global X and Y direction at depth X, respectively; u_{sh} is the soil shear displacement magnitude; X_{sh} is the depth in the middle of the shear plane; and b_{sh} is a parameter governing the thickness of the shear zone. In this formulation, the bottom half of the soil slides away from the stationary top half (typical shear box conditions). However, this is kinematically similar to the case where the top half slides and the bottom half is stationary.

The soil displacement can now be expressed in the local coordinate system of a root segment:

$$\begin{bmatrix} u_s \\ w_s \end{bmatrix} = \boldsymbol{R}(\Theta_0) \begin{bmatrix} U_s \\ W_s \end{bmatrix}, \tag{25}$$

where Θ_0 is the orientation of the nondisplaced root segment in the global coordinate system, and $\boldsymbol{R}$ is a rotational matrix:

$$\boldsymbol{R}(\theta) = \begin{bmatrix} \cos\theta & \sin\theta \\ -\sin\theta & \cos\theta \end{bmatrix}. \tag{26}$$

In the model, the soil behaviour is only taken into account as an external load acting on the root. This adds a complication to the definition of relative root-soil displacement, as the soil strain is not explicitly tracked during the analysis. The soil-root resistance will depend on the deformation history of the unit of soil present at the deformed position of the root rather than the original root position. To take this into account, the relative soil-root displacement is defined as follows; see Figure 6A. First, soil displacements u_s and w_s are calculated at the deformed position of the root (C) using Equation 25 and subsequently expressed in a coordinate system aligned with the deformed root segment to find soil displacements u_s' and w_s'. Because the direction of soil displacement (θ_{sh}, expressed in the local coordinate system *x-y*) is known, the original

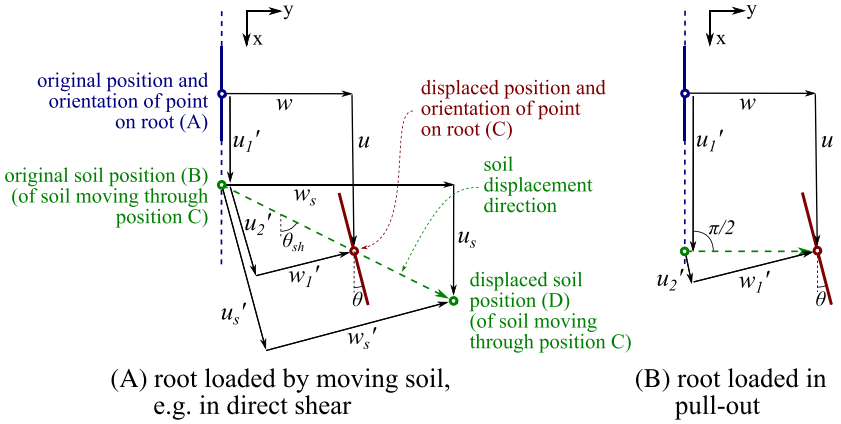

FIGURE 6 Schematisation of relative soil-root displacement. A point on the root displaced from position "A" to position "C." The soil that interacts with the displaced root has moved from original position "B" to displaced position "D" along a path aligned with the soil displacement orientation θ_{sh} and passing through position "C" [Colour figure can be viewed at wileyonlinelibrary.com]

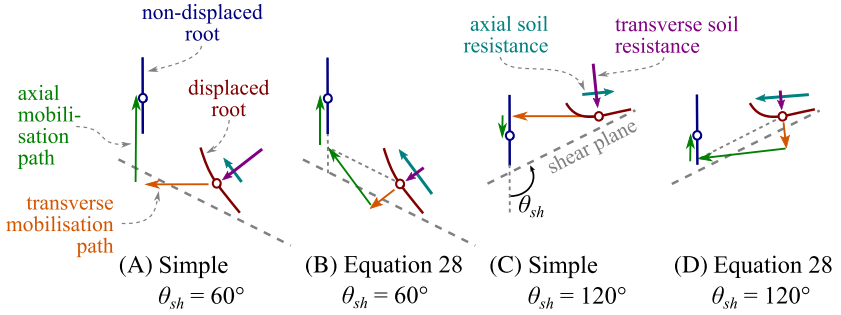

FIGURE 7 Schematic representation of the effect of the assumed mobilisation path on the direction and magnitude of the soil resistance. The investigated point on the root is located above the shear plane, so $u_s = w_s = 0$ mm. "Simple" mobilisation assumes that $\Delta u = u_s - u$ and $\Delta w = w_s - w$ [Colour figure can be viewed at wileyonlinelibrary.com]

(B) and the displaced position (D) of the soil affecting the behaviour of the displacement root (at position C) can then be found. Subsequently, the root displacement is found, which consists of two parts. Initially, the root is modelled as moving axially from A to B (u_1'). Then root rotation θ takes place. Hereafter, the root moves axially (u_2') and transversely (w_1') to reach the deformed root position C. The relative root-soil displacements can now be expressed as the difference in axial and transverse deformations between the soil and the root:

$$\begin{bmatrix} \Delta u \\ \Delta w \end{bmatrix} = \begin{bmatrix} u_s' - (u_1' + u_2') \\ w_s' - w_1' \end{bmatrix} = \boldsymbol{R}(\theta) \begin{bmatrix} u_s - w\cot\theta_{sh} \\ w_s - w \end{bmatrix} + \begin{bmatrix} w\cot\theta_{sh} - u \\ 0 \end{bmatrix}. \tag{27}$$

It is necessary to adopt such a relatively complicated definition for the mobilisation distance, rather than, for example, simply assuming $\Delta u = u_s - u$ and $\Delta w = w_s - w$, because of the potentially large root deformations. For example, in the case when the angle between root and shear plane is large ($\theta_{sh} > 90°$), when using such a simple formulation, the direction of the axial soil resistance might incorrectly reverse for certain parts of the root; see Figure 7. The validity of the mobilisation path described by Equation 27 will be investigated later in this paper.

In the case of pull-out loading, the soil was assumed to remain stationary: $u_s = w_s = 0$. Furthermore, the soil displacement orientation θ_{sh} was assumed perpendicular to the nondisplaced root ($\theta_{sh} = \pi/2$); see Figure 6B. Therefore, in the case of pull-out loading, Equation 27 can be simplified to

$$\begin{bmatrix} \Delta u \\ \Delta w \end{bmatrix} = \begin{bmatrix} -u_1' - u_2' \\ -w_1' \end{bmatrix} = \boldsymbol{R}(\theta) \begin{bmatrix} 0 \\ -w \end{bmatrix} + \begin{bmatrix} -u \\ 0 \end{bmatrix}. \tag{28}$$

2.6 | Boundary conditions

To find the displaced position of a single root segment, the set of differential Equations 4-7 has to be solved simultaneously. Every set has six unknowns. When the root architecture contains multiple segments (eg, a main root with some side branches), all sets have to be solved simultaneously. Assuming n segments, this leads to a set of $4n$ differential equations with $6n$ unknowns. Therefore, $6n$ boundary equations are required.

Two types of nodes were distinguished to define coupling between segments (ie, root system architecture): (1) root end nodes: nodes to which only one segment connects and (2) root "middle" nodes: nodes to which multiple segments connect (Figure 2). At a free root end node (not supported in any way), internal root forces have to be zero. This provides three boundary equations: $N = 0$, $V = 0$, and $M = 0$. When a root end node is constrained in any degree of freedom, one or more of these changes into a constraint on root displacement. At root "middle" nodes, when they are "free" (ie, not having any external constraints in any degree of freedom) internal forces in all degrees of freedom have to be in equilibrium, resulting in another three boundary conditions per "middle" node. Furthermore, at every "middle" node, the global root displacements have to be equal for every connecting segment. This yields another $3(n_s - 1)$ boundary conditions per "middle" node (n_s is the number of connecting segments to the node). This results in sufficient boundary conditions to solve the full set of equations.

2.7 | Numerical implementation

As the system of equations is too complicated to solve analytically, the (open source) Python programming language is used to solve the problem numerically, using a boundary value problem solver (`solve_bvp`) from the `integrate` package within the `scipy` library.[19]

The problem is solved in a nonincremental fashion, ie, the system of equations is solved directly for any given value of soil displacement u_{sh}. However, the solver struggles to find the solution for larger values of u_{sh} because of difficulties making a good initial guess. Therefore, such larger deformation problems were solved incrementally using runs with increasing values of u_{sh}, using the solution of the last run as the initial guess for the new run. The initial guess for the first run was no assumed displacement.

2.8 | Calculation of root-reinforcement

When the model is used to predict shear reinforcement by roots, the reinforcement (F_r) is defined as the sum of forces acting in the direction of shearing and the additional resistance against shearing caused by an increase in normal pressure on the shear plane (compare Equation 2):

$$F_r = \sum_i \left(F_{parallel,i} + F_{perpendicular,i} \tan \phi_{cv} \right), \tag{29}$$

where $F_{parallel,i}$ and $F_{perpendicular,i}$ are the forces in root segment i parallel and perpendicular to the shear plane, respectively. Both forces can easily be calculated using the root internal forces (N and V) in the middle of the shear plane and the angle between the deformed root and the shear plane. The critical state angle ϕ_{cv} is used in Equation 29 rather than the peak friction angle because roots typically mobilise their strength at relatively large displacements compared with the soil (eg, other studies[20-22]). In the case of vertical pull-out, static equilibrium of forces is assumed at the node at which the pull-out displacement is prescribed. The pull-out force can therefore be found by summing the vertical components of the axial and shear force at this node.

2.9 | Nondimensionalisation

The system of equations can be nondimensionalised by dividing over root diameter d. Roots are assumed to have circular-shaped cross sections, so $A = \pi d^2/4$ and $I = \pi d^4/64$. Defining $s = \hat{s}d$, Equations 4 and 5 can be written as

$$-\frac{q_a}{E_t d} = \frac{\pi}{4}\frac{\mathrm{d}\epsilon_a}{\mathrm{d}\hat{s}} + \frac{\pi}{64}\frac{E_b}{E_t}\frac{\mathrm{d}^2\theta}{\mathrm{d}\hat{s}^2}\frac{\mathrm{d}\theta}{\mathrm{d}\hat{s}}, \tag{30}$$

$$\frac{\pi}{64}\frac{E_b}{E_t}\frac{\mathrm{d}^3\theta}{\mathrm{d}\hat{s}^3} = \frac{q_l}{E_t d} + \frac{\pi}{4}\epsilon_a\frac{\mathrm{d}\theta}{\mathrm{d}\hat{s}}. \tag{31}$$

This yields the first of the nondimensional parameter groups governing the problem: root stiffness ratio $E_b E_t^{-1}$. Axial and lateral loading terms can be rewritten into

$$\frac{q_a}{E_t d} = \pi\zeta_a\frac{\tau_u}{E_t}, \tag{32}$$

$$\frac{q_l}{E_t d} = \zeta_l\frac{p_u}{E_t d}, \tag{33}$$

resulting in two further groups: $\tau_u E_t^{-1}$ and $p_u E_t^{-1} d^{-1}$. When soil and root displacements are also normalised by diameter d, the mobilisation parameters ζ_a and ζ_l can be expressed as

$$\zeta_a = \tanh\left(\frac{\Delta\hat{u}d}{b_a}\right), \tag{34}$$

$$\zeta_l = \tanh\left(\frac{\Delta\hat{w}d}{b_l}\right), \tag{35}$$

yielding two nondimensional strength mobilisation parameters $b_a d^{-1}$ and $b_l d^{-1}$. The soil displacement profile (Equation 24) can equally be rewritten in terms of nondimensional parameter group $b_{sh} d^{-1}$. The final nondimensional group is the root slenderness (Ld^{-1}), which will affect the root behaviour through boundary conditions.

3 | MODEL VALIDATION

The model was validated against three sets of laboratory experiments using root analogues:

- Experiment A: Direct shear box testing in dry, medium dense sand reinforced with plastic root analogues.[15]
- Experiment B: Direct shear box testing in dry, very dense sand reinforced with rubber or wooden root analogues.[14]
- Experiment C: Pull-out testing in dry or partially saturated sand reinforced with rubber or wooden root analogue systems with various architectures.[23]

3.1 | Experiment A: Direct shear testing in dry sand with plastic root analogues

3.1.1 | Material and methods

Liang et al[15] performed direct shear tests in a large (300 × 300 × 270 mm) shear box reinforced with 3D-printed ABS root analogues. The shear plane was located at 75 mm depth, and the effective vertical stress on the shear plane was 4.0, 8.0, or 12.0 kPa.

Each box was reinforced with one 12 mm, six 3 mm, and two 1.6 mm diameter root analogues each with a length of 150 mm. All root analogues were vertically placed with the top of the analogue at the soil surface level and spaced far apart ($s/D > 8$) to avoid root-soil-root interaction. The material behaviour in tension can be approximated using a linear stiffness up to yielding at approximately 2.5% strain (see stress-strain curves by Liang et al[15]). The tensile stiffness E_t (in MPa) varies as a function of root diameter d [24]:

$$E_t \approx 3602\left(\frac{d}{d_{ref}}\right)^{-0.606}, \tag{36}$$

where $d_{ref} = 1$ mm. In model simulations, it was assumed that the bending stiffness E_b is equal to the tensile stiffness E_t.

Dry, medium dense HST 95 Congleton silica sand was used (relative density $I_d = 55\%$ to 60%; $d_{50} = 0.1$ mm), corresponding with a dry unit weight of $\gamma' \approx 16.5\,\mathrm{kNm}^{-3}$. The critical state friction angle[25] was $\phi_{cv} = 32°$. Assuming a shear plane thickness[26] of $10d_{50}$, the hyperbolic tangent shear plane parameter b_{sh} was chosen as 0.34 mm. This corresponds with 90% of the shear displacement step change occurring over the shear plane thickness. The coefficient of lateral pressure required to calculate the axial resistance along the root analogue was assumed to be $K = K_0 = 1 - \sin\phi'$. ϕ' was chosen as ϕ_{cv}, similar to Liang et al.[15]

It is assumed that root analogues do not affect each other due to the large spacing, and so the reinforcement contribution from each root analogue was superimposed to predict the overall root-reinforcement in the shear tests.

3.1.2 | Results

The modelled reinforcement was close to the reinforcement measured and modelled by Liang et al[15] (Figure 8). The model captures the initial very stiff response of the reinforcement ($0 \leq u_{sh} \lessapprox 1$ mm), followed by a zone of reduced stiffness ($1 \lessapprox u_{sh} \lessapprox 10$ mm), followed by a shear displacement range in which the reinforcement is more or less constant

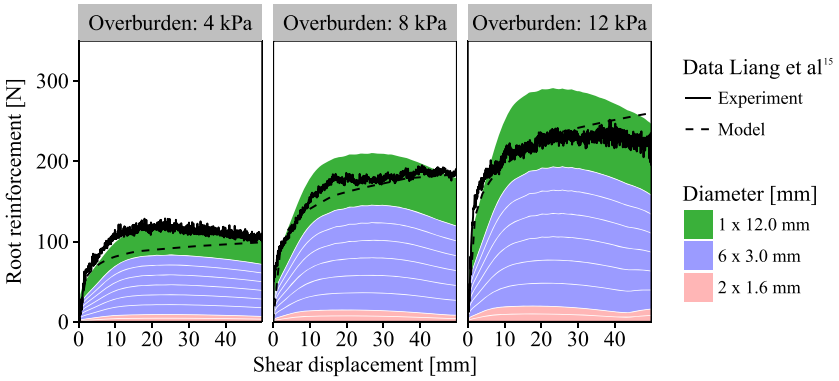

FIGURE 8 Modelled and measured root-reinforcement in direct shear tests by Liang et al.[15] The sum of individual root contributions (shaded areas) represents the total modelled reinforcement using the proposed model [Colour figure can be viewed at wileyonlinelibrary.com]

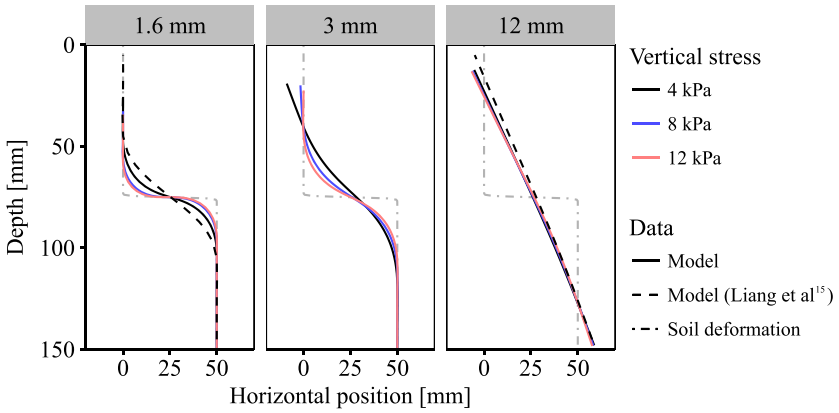

FIGURE 9 Root shapes after 50 mm shear displacement. The dash-dot line indicates the assumed soil displacement profile. Data by Liang et al[15] only available for 1.6 and 12 mm roots under 4 kPa normal stress [Colour figure can be viewed at wileyonlinelibrary.com]

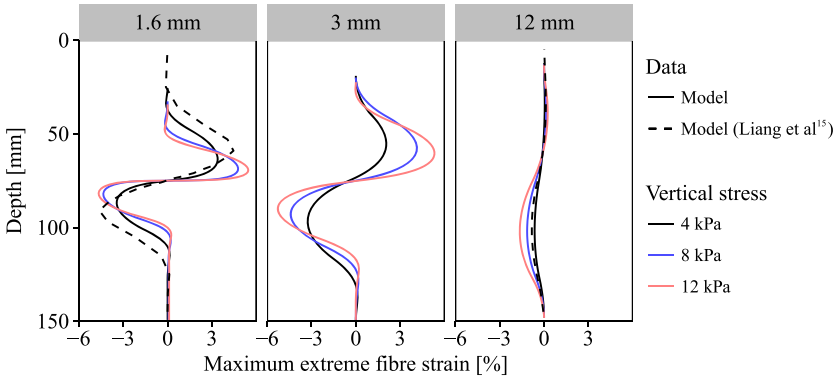

FIGURE 10 Axial strain in the extreme root analogue fibre after 50 mm soil shear displacement. Data by Liang et al[15] only available for 1.6 and 12 mm roots under 4 kPa normal stress [Colour figure can be viewed at wileyonlinelibrary.com]

($u_{sh} \gtrapprox 10$ mm). The predicted root shape (Figure 9) and root strain (Figure 10) at 50 mm shear displacement are similar to their model predictions. This should not come as a major surprise, because their modelling approach, using more detailed *p-y* curves and using finite elements to solve the beam-spring interaction problem within ABAQUS, was similar to the simplified approach suggested in this paper. In contrast to the model proposed here, however, the model by Liang et al[15] did not consider axial components. The similarity between the two models suggests that the ABS root analogues mainly reinforce the soil through bending in these tests. This can now be confirmed by our model, which shows that the axial strain is one to two orders of magnitude smaller than the bending strain. This indicates that for roots of similar stiffness, where bending dominates the response, neglecting the axial components is acceptable.

In the proposed model, displacements and strains were concentrated closer to the shear plane. This could be due to the orientation of root forces: in the model described herein, the axial and transverse soil-root resistance work parallel and perpendicular to the *deformed* root orientation, while in the model by Liang et al[15] the transverse resistance acts perpendicular to the *nondisplaced* root orientation.

3.1.3 | Sensitivity to model assumptions

The shear band thickness could not be measured during the test and was therefore assumed as $10d_{50}$. However, the presence roots may have widened the shear band through redistribution of load, as observed in direct shear tests on soil reinforced with artificial fibres.[27] To test the sensitivity of the model predictions to the shear band thickness, additional simulations for individual roots in tests with 8 kPa vertical stress were run with shear bands ranging from 1 to 40 mm (Figure 11). For 1.6 mm diameter root analogues, with increasing shear band thickness, both the maximum reinforcement and the rate of mobilisation decreased but only when the shear band thickness exceeded 20 mm ($200d_{50}$). For thicker roots, the influence of the shear band thickness was much smaller. This analysis shows that small uncertainties in the assumed shear band thickness ($10d_{50} = 1$ mm) will not have affected the direct shear tests predictions significantly.

A similar sensitivity study was performed for the effect of axial friction. The coefficient of lateral earth pressure K was varied from $0.5K_0$ to $4.0K_0$. Larger confining stresses increased the peak root reinforcement for all roots (Figure 12).

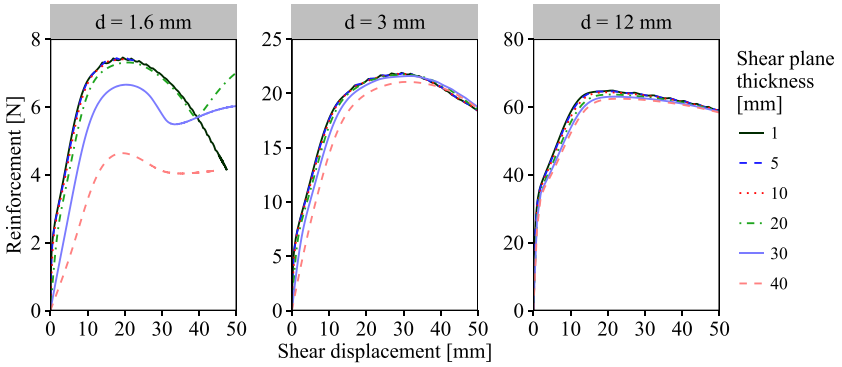

FIGURE 11 Effect of shear band thickness assumption on the predicted behaviour of single acrylonitrile butadiene styrene (ABS) roots in the case of 8 kPa vertical stress [Colour figure can be viewed at wileyonlinelibrary.com]

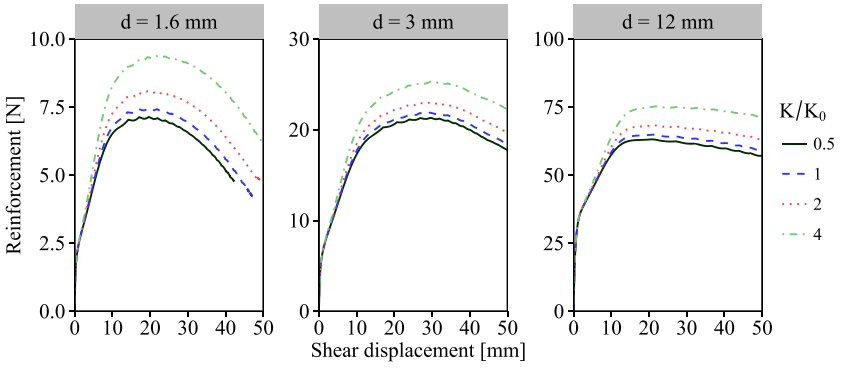

FIGURE 12 Effect of lateral earth pressure on the predicted behaviour of single acrylonitrile butadiene styrene (ABS) roots in the case of 8-kPa vertical stress [Colour figure can be viewed at wileyonlinelibrary.com]

Interestingly, the initial reinforcement "stiffness" was hardly affected, because this initial behaviour is largely governed by the mobilisation of transverse rather than axial resistance along the root. It can be concluded that small errors in the axial friction assumptions will only have had a very small effect on the modelled shear box tests.

3.1.4 | Validation of resistance mobilisation

The proposed model uses a nonincremental approach to define the mobilised soil resistance, using the simplified displacement path assumed by Equation 27. To check the validity of this assumption, these simplified "direct" paths were compared with incrementally determined paths. The latter were found by summing the incremental axial and transverse displacement components between deformed positions found using the "direct" approach. Figure 13 shows these paths and the effect on mobilisation parameters ζ_a and ζ_l for $d = 1.6$ and $d = 12$ mm ABS root analogues under 4 kPa normal stress for a point originally located 15 mm above the shear plane. The results show that, despite the direct and incremental paths being slightly different, the effect on the resistance mobilisation is small. This can be easily understood by observing that the relative soil-root displacements are large compared with the displacement required to mobilise resistance ($\Delta u \gg b_a$, $\Delta w \gg b_l$). Therefore, it was concluded that the main function of mobilisation displacement Equations 27 and 28 is to ensure that soil resistance is present at the right place along the root (wherever the relative soil-root displacement is finite) and to ensure that this resistance is oriented correctly.

3.2 | Experiment B: Direct shear testing in dry sand with rubber and wooden root analogues

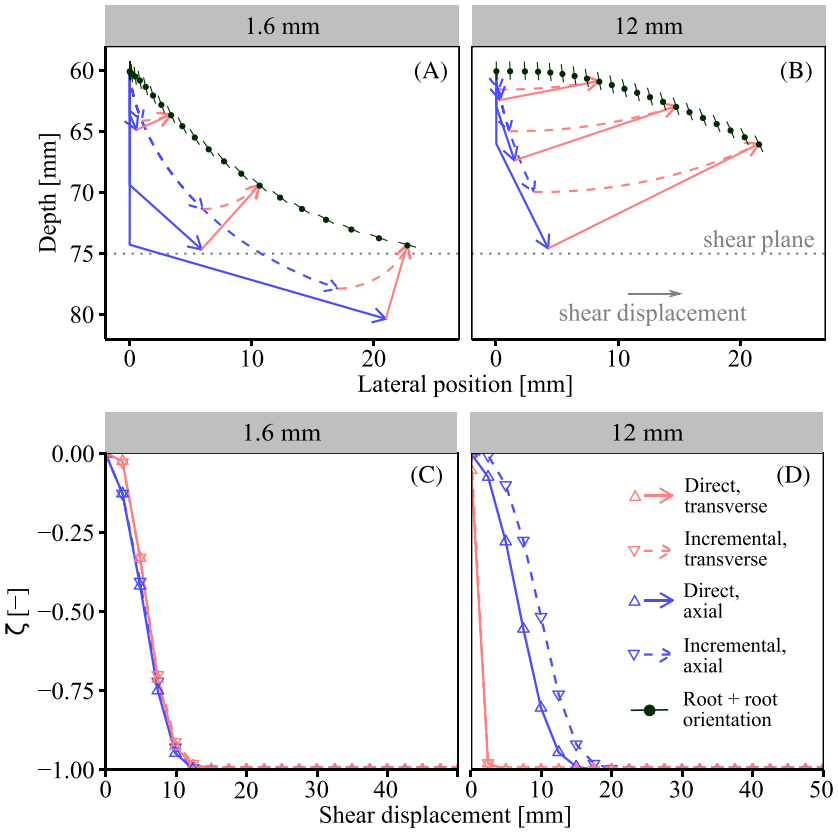

FIGURE 13 Root displacement and fraction of resistance mobilised (ζ) for a point on the root at an initial depth of $X = 60$ mm for a $d = 1.6$ and $d = 12$ mm ABS root analogue under a normal stress of 4 kPa. Shear displacements steps are 2.5 mm [Colour figure can be viewed at wileyonlinelibrary.com]

3.2.1 | Material and methods

Duckett[14] performed direct shear tests in a cylindrical (100 mm diameter) shear box reinforced with Viton O-ring rubber root analogues (RS Components) or beech wooden dowels. The shear plane was located at 50 mm depth, and no overburden pressure was applied. The top of the root analogues was located at the soil surface. Cardboard disks were glued to the top of the root analogues to prevent them from slipping into the soil during shearing, thus modelling the constraint introduced by the aboveground part of the plant. In the proposed model, this was incorporated by fixing the vertical degree of freedom at the topmost part of the root analogue ("clamped" cases). To study the effect of clamping, separate model simulations were performed modelling a free end at the topmost part of the root analogue ("unclamped" cases).

The diameter of the rubber was either 1.6 or 3.0 mm, and the diameter of all wooden root analogues was 3.0 mm. All analogues had a length of 150 mm. Root analogues were vertically placed in the box in various configurations (Figure 14), and for every configuration, including the case with no root analogues, three replicates were tested. The reinforcement was found by subtracting the average nonrooted soil resistance from the measured total shear resistance. In the model simulations, no root-soil-root interaction was assumed, so a prediction for an experiment could be made by superimposing the modelled force-displacement trace of every root analogue in the test.

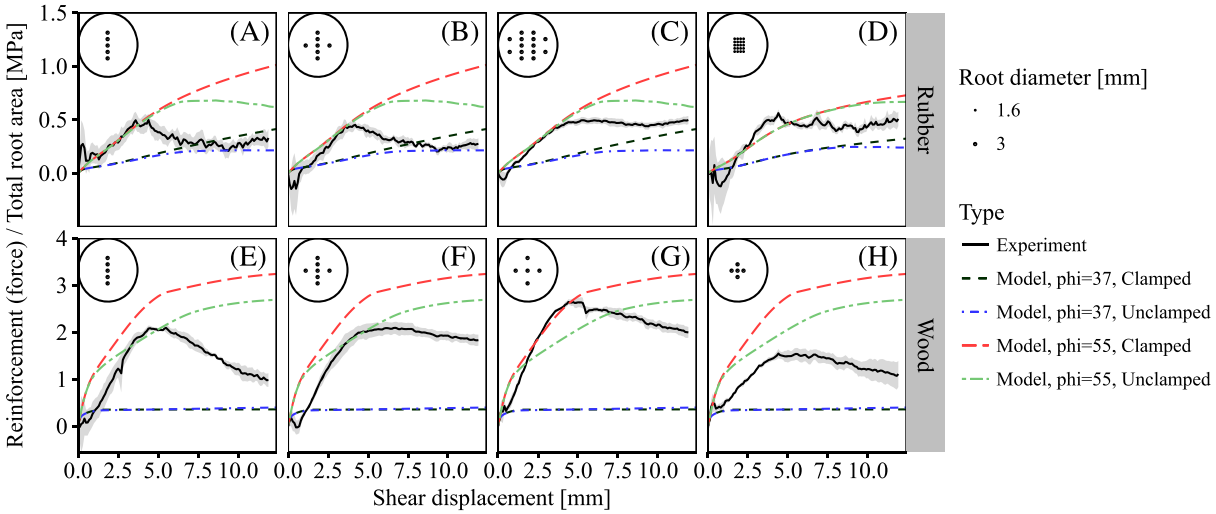

FIGURE 14 Experimental and model results of shear box tests by Duckett.[14] Shaded areas indicate the standard error of the mean for experimentally measured values (three tests per root configuration). Reinforcement (*y*-axis) is defined as the difference between rooted and unrooted tests. Note that the reinforcement is given per unit cross-sectional area of root analogue [Colour figure can be viewed at wileyonlinelibrary.com]

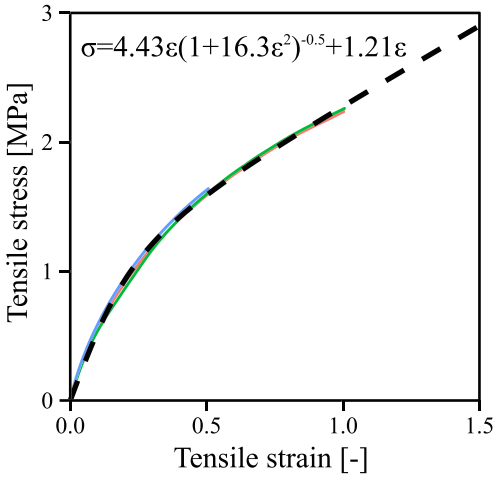

FIGURE 15 Tensile tests on 3 mm diameter Viton rubber. Individual tests are represented by different colours [Colour figure can be viewed at wileyonlinelibrary.com]

The stiffness of the $d = 3$ mm rubber was tested in tension and the stiffness of the wood in 3-point bending. Because both were non-linear (Figures 15 and 16), the secant stiffness was fitted using an empirical best-fit curve of the following form:

$$E_{sec} = \frac{\sigma}{\epsilon} = \frac{\xi_1}{\sqrt{1 + \xi_2 \epsilon^2}} + \xi_3. \tag{37}$$

For rubber, fitted parameters are $\xi_1 = 4.43$ MPa, $\xi_2 = 16.3$ [-], and $\xi_3 = 1.21$ MPa. For the wood, $\xi_1 = 20074$ MPa, $\xi_2 = 7798$ [-], and $\xi_3 = 0.0$ MPa. The tensile strength of the rubber could not be determined from the test data as the material was still intact at the maximum tested tensile strain of $\epsilon = 1$. For calculating the tensile stiffness (E_t) in the model, $\epsilon = \epsilon_a$, while for calculating the bending stiffness (E_b), $\epsilon = 0.5\kappa d = 0.5d(\mathrm{d}\theta/\mathrm{d}s)$ was used.

Duckett[14] performed shear tests in dry, very dense Redhill 110 sand ($I_d = 89\%$) at a dry unit weight of 16.6 kNm^{-3}. The critical state and peak friction angles were measured as $\phi_{cv} = 37°$ and $\phi' = 55°$, respectively, using a conventional 60 × 60 mm square shear box (Figure 17). Two sets of model simulations were run: one with critical state parameters ($\phi' = \phi_{cv} = 37°$ and one based on peak parameters ($\phi' = 55°$, $\phi_{cv} = 37°$). Interface friction angles for rubber and wood were not experimentally determined and were assumed to be $\delta = 0.75\phi'$ based on values for ABS in Experiment A.

The sand was very dense and the confining stresses very low ($\sigma'_v < 2.5$ kPa), and so, during pull-out, some dilation will have occurred. This dilation will have increased the radial stress around the root and therefore the axial soil-root interface resistance. To take this into account, the coefficient of lateral earth pressure was assumed to be equal to the coefficient for the passive case: $K \approx K_p = (1 + \sin\phi_{cv})/(1 - \sin\phi_{cv}) = 4.02$.

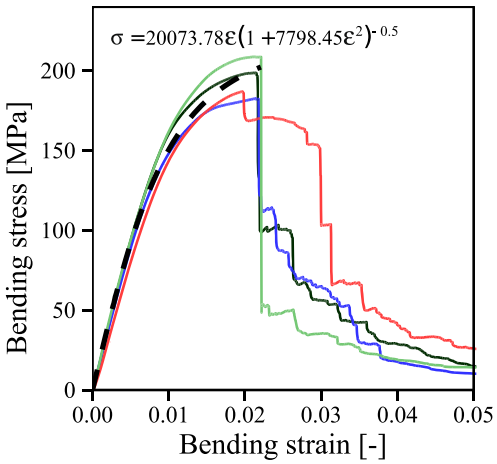

FIGURE 16 Three-point bending tests on 3-mm diameter beech dowels. Individual tests are represented by different colours [Colour figure can be viewed at wileyonlinelibrary.com]

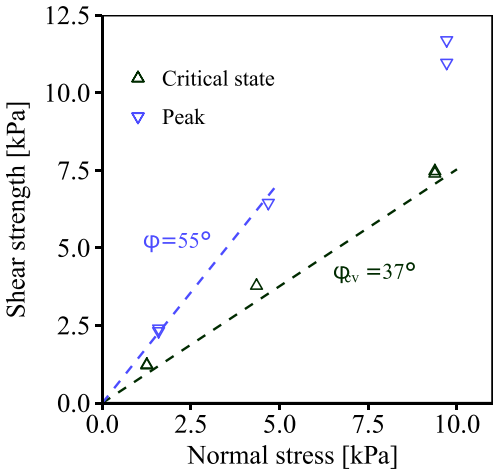

FIGURE 17 Direct shear results for dry Redhill 110 sand at a relative density of $I_d = 89\%$ [Colour figure can be viewed at wileyonlinelibrary.com]

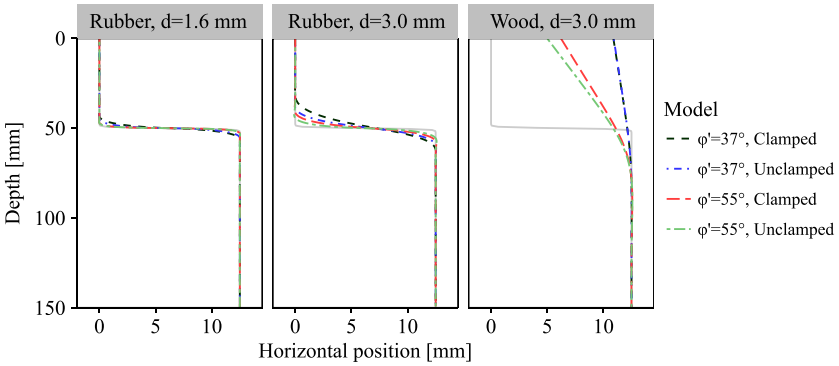

FIGURE 18 Deformed root positions after 12.5 mm shear displacement. The solid grey line indicates the assumed displaced soil position [Colour figure can be viewed at wileyonlinelibrary.com]

3.2.2 | Results

None of the root analogues was broken after the maximum shear displacement of 12.5 mm was reached. Wooden analogues provided more reinforcement than rubber ones per unit root cross-sectional area (Figure 14). This could be explained by their greater strength. Furthermore, their resistance is mobilised quicker due to their greater stiffness.

There was some initial compliance in the shear box or slack in the analogues, as the reinforcement generally mobilised after approximately 0.5 mm shear displacement. When this compliance is ignored, the model using the peak soil friction angle matched the experimentally measured reinforcement gradient well at the start of the test for both analogue materials. After approximately 4 to 5 mm shear displacement, however, the experimentally measured reinforcement softened towards model predictions based on the critical state friction angle. This suggests that for larger shear displacements, reinforcement predictions should be made using soil critical state parameters rather than peak parameters. In the field, stress levels will be greater (such as in Experiment A), displacements larger (such as in Experiment C), and soil densities smaller. Therefore, calculating axial and transverse root resistance using critical state parameters is likely be more appropriate in these cases.

For rubber root analogues, the effect of clamping the topmost part of the root analogue only started to have an effect after shear displacement $u_{sh} \approx 10\,\text{mm}$ ($d = 1.6\,\text{mm}$) or $u_{sh} \approx 6\,\text{mm}$ ($d = 3.0\,\text{mm}$). At greater deformations, the unclamped roots simply slipped, causing the reinforcement to stay more or less constant, while clamped roots continued to mobilise more reinforcement. For wooden root analogues, this threshold displacement was much smaller ($u_{sh} \approx 1\,\text{mm}$), and unclamped roots continued to mobilise resistance beyond this point, albeit less than clamped roots.

The model showed clear differences in the root shapes after the maximum shear displacement has been reached (Figure 18). Flexible rubber analogues followed the soil shear displacement profile closely, while stiffer wooden analogues behaved more like rigid piles. This figure also shows that the root deformation followed the soil deformation more closely when the axial confinement was small (unclamped cases) or the transverse confinement was large ($\phi' = 55°$).

Closer root spacing has a negative effect on the reinforcement, as can be seem by comparing Figure 14G (spacing s/root diameter $d = 6.67$) to Figure 14H ($s/d = 3.33$). This can be explained by root-soil-root interaction.

3.3 | Experiment C: Pull-out testing of root analogues

3.3.1 | Material and methods

Mickovski et al[23] performed pull-out tests on rubber and wooden root analogues in dry and partially saturated sand. The diameter of the Viton rubber root analogues was 1.7 mm. Although Mickovski et al[23] used a tensile stiffness of 28.7 MPa, this appears unrealistically high and experimentally measured values from Experiment B were used instead. The diameter of the wooden dowels (Linden wood) was 2.3 mm, and their Young's modulus was 1264 MPa.[23]

Three root architectures were considered: (*a*) tap, (*b*) herringbone, and (*c*) dichotomous branching (Figure 19). Each root analogue protruded 10 mm above the soil surface. In the model simulations, the pull-out force was applied to the topmost point of the root.

The same sand at the same dry density was used as in Experiment B. Pull-out tests were conducted in both fully dry sand and partially saturated sand ("wet"). In the latter case, samples were first fully saturated and then drained under an hydraulic head of −450 mm at the surface. The water retention characteristics of the sand are unknown, and it was

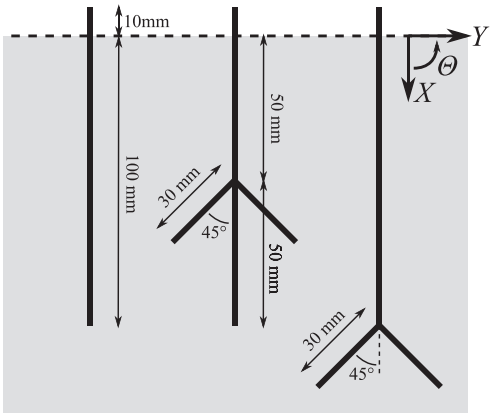

FIGURE 19 Root architectures used in pull-out tests by Mickovski et al[23]

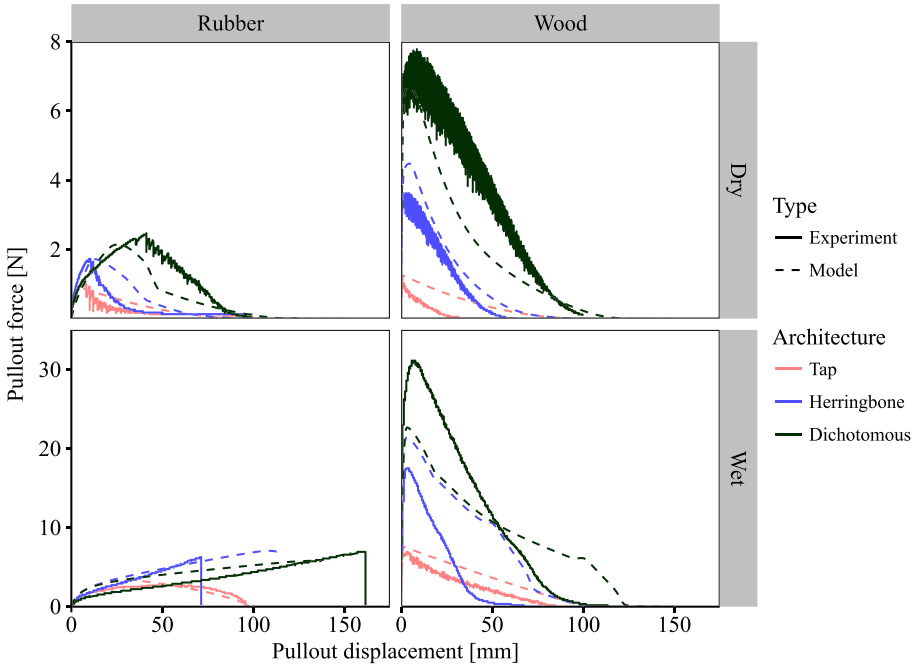

FIGURE 20 Measured and predicted pull-out force-displacement traces for rubber and wooden root analogues in dry and wet (partially saturated) sand. Experimental data from Mickovski et al[23] [Colour figure can be viewed at wileyonlinelibrary.com]

assumed that the suction was below the air-entry value, so that the increase in vertical effective stress equals the change in suction (ie, $\chi = 1$; eg, Fredlund and Rahardjo[28]). The vertical effective stress with depth can then be modelled using Equation 10 and adopting $\sigma'_{v,0} = 4.5\,\text{kPa}$ (suction effect) and $\gamma' = \gamma_{sat} - \gamma_w$, where γ_{sat} is the saturated unit weight ($20.1\,\text{kNm}^{-3}$) and γ_w the unit weight of water.

Similar to Experiment B, $\delta = 0.75\phi'$ and $K = K_p$ were assumed because of the high relative density of the soil. Analyses were run using critical state parameters rather than soil peak parameters due to the large pull-out displacements.

3.3.2 | Results

The modelled pull-out force-displacement traces matched the experimentally determined traces well for both rubber and wooden root analogues (Figure 20). Some discrepancies began to occur at larger displacements. It is hypothesised that this is caused by a change in the failure mechanism of the soil around the root branches as these approach the soil surface (note the large relative root-soil deformations in Figure 20).

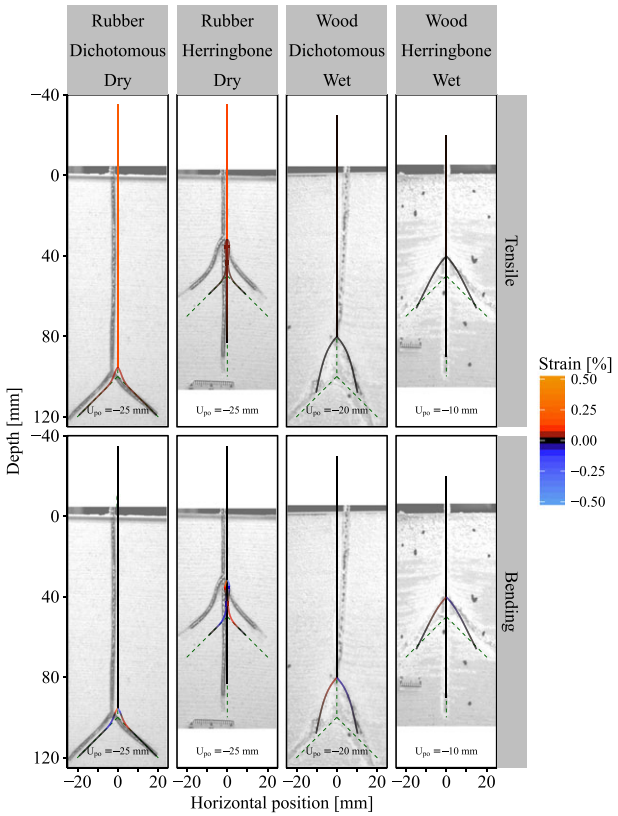

FIGURE 21 Measured and modelled shape and strain in root analogue after a displacement of U_{po}. Green dashed lines indicate the original position of the root (model). Images from original data files of Mickovski et al[23] [Colour figure can be viewed at wileyonlinelibrary.com]

The least accurate predictions were made for branched, wooden analogues in partially saturated sand. Under these conditions, the model results for dichotomous and herringbone branched roots almost yielded the same peak pull-out forces. This reflects the assumed effective stress conditions; the assumed vertical stress at 50 mm depth ($\sigma'_v \approx 5.0$ kPa) is almost equal to the assumed stress at 100 mm depth ($\sigma'_v \approx 5.5$ kPa). The difference with the experimental results is attributed to unsuitability of the chosen soil transverse resistance model for partially saturated soil, as the model by Reese and Van Impe[16] was validated against laterally loaded piles in fully saturated conditions only.

The herringbone and dichotomous rubber roots in wet soil were reported by Mickovski et al[23] to have broken during testing, explaining the sudden loss in pull-out resistance. As the tensile strength of the rubber was not known and therefore not implemented in the model, such a drop is not visible in the model results.

For all tap roots, the close match between measured and predicted peak forces suggests that the assumption $K \approx K_p$ was reasonable. Increases in confining stress during pull-out have been observed previously (eg, Lehane and White[29]).

The predicted deformed shapes of the root analogues were similar to the ones observed during pull-out of half cross-section root analogues placed against a perspex viewing window[23]; see Figure 21. The model shows that the axial strain in side branches was relatively small compared with the axial strain in the main root, especially for wooden root analogues. Bending strains in the side branches were relatively large, especially near the branching point. This shows that additional pull-out resistance introduced by side branches for a significant part stems from transverse rather than axial soil resistance, even in very flexible materials such as the rubber root analogues.

4 | DISCUSSION AND CONCLUSIONS

The validation against experimental data shows that the proposed model can be used on root analogues with widely ranging stiffnesses (wood, plastic, and rubber), soil stresses typical for roots growing near the soil surface (0 to 12 kPa vertical effective stress), architectures (unbranched and branched), and loading conditions (direct shear and pull-out). It should be noted that this range of root analogue stiffness properties and diameters brackets those of a wide range of root species.

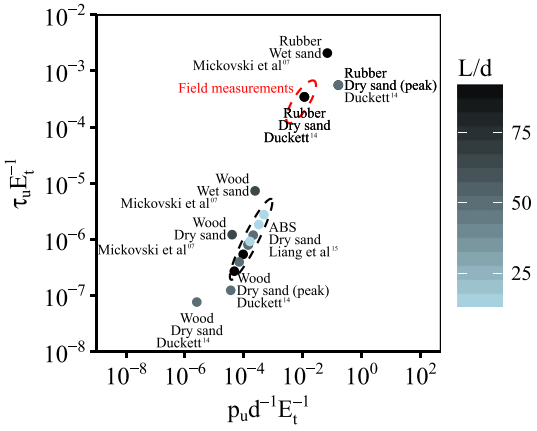

FIGURE 22 Comparison of dimensionless parametric groups for laboratory experiments and field data. Field data based on estimations of p_u and τ_u using cone penetration tests (CPT) and shear vane testing in clayey silt rooted with Pedunculate oak and sandy silt rooted with Sitka spruce. E_t was measured by uniaxial tension tests[30] [Colour figure can be viewed at wileyonlinelibrary.com]

Seven nondimensional parametric groups governing the problem were identified. These all have a physical meaning and can be measured or estimated using root biomechanical data and soil properties. Because the axial and lateral soil-root resistance mobilises relatively quickly compared with typical root displacements, the influence of $b_a d^{-1}$ and $b_l d^{-1}$ is likely to be small. In this work, it was assumed that roots do not affect the soil displacement profile (constant $b_{sh} d^{-1}$) because the number of roots was low. Assuming that the tensile strength of root analogues was similar to the bending strength, it was hypothesised that differences between analogues largely stemmed from different values of $\tau_u E_t^{-1}$, $p_u E_t^{-1}$ (which spanned several orders of magnitude; see Figure 22) and root slenderness Ld^{-1}. All tests using wooden and ABS root analogues had small values for dimensionless groups $p_u d^{-1} E_t^{-1}$ and $\tau_u E_t^{-1}$ compared with cases with real tree and woody shrub roots in field conditions measured by Meijer et al.[30,31] Tests using rubber root analogues in shallow, dry sand were closer to field conditions; the small tensile stiffness of rubber compared with real roots was offset by the small soil resistances. All root analogues tests were short compared with typical root length-diameter relationships. For example, for Norway spruce,[32]

$$L \approx 390 \left(\frac{d}{d_{ref}} \right)^{0.56}, \tag{38}$$

where $d_{ref} = 1$ mm. Compared with real roots, the modelled root analogues were axially less constrained due to limited root lengths. This will have resulted in larger axial deformations and more axial root "slippage."

A number of key model assumptions are made in the model that need to be addressed in future work:

1. The root behaviour has no influence on the soil behaviour (the shear displacement profile is an input parameter in the model), so the shape of the shear displacement profile is independent of roots. This is a valid assumption when roots are sparse and the root area ratio (*RAR*, ratio of cross-sectional area of root over cross-sectional area of soil) is small, so that the reinforcement is relatively small compared to the soil shear component. For rooted soil near the surface, *RAR* typically does not exceed 1% to 2%. From previous tests, however, it is known that the thickness of the shear band might increase due to roots/fibres (eg, Shewbridge and Sitar[27]). A thicker shear band means the root-reinforcement might be mobilised more gradually as relative root-soil displacements are smaller. The proposed model does account for a finite thickness of the shear band (which can be manually changed), although it is not explicitly incorporated into the root-soil interaction.
2. The transverse and axial ultimate resistances p_u and τ_u are calculated assuming vertical roots in fully saturated, fully drained purely frictional soil. Future work should focus on the effect of root orientation, unsaturated conditions (suctions), and loading rates (drained or undrained behaviour) on the magnitude of the soil resistance on the root.
3. In the current version of the model, root failure was not introduced because most of the experimentally tested root analogues did not fail. Future versions should include a failure criterion based on real root behaviour, as real roots may break when loaded in shear or pull-out. Although information on root uniaxial tensile behaviour is commonly measured, (eg, Mao et al[4]), no reliable data for other failure modes (bending, shear, or interactions) is available and should be collected for real roots.

The model validation is inconclusive on whether peak or critical state soil parameters should be used. Direct shear tests in medium dense sand (Experiment A) and pull-out tests in very dense sand (Experiment C) suggest critical state behaviour, while the relatively large direct shear reinforcements in very dense sand suggest peak parameters work better initially, with critical state reached at larger displacements (eg, in catastrophic landsliding). In the field, however, rooted soils have relatively low densities because roots only grow near the surface (typically in the top 0.5 m[33]). Furthermore, root growth is limited in soils with penetration resistances exceeding 2 MPa.[34] Thus, in real field cases, critical state parameters are likely to be more appropriate.

As for any soil model, choosing realistic input parameters is of the utmost importance. All input parameters for this model are based on physical properties of roots and soil. Root properties can be derived from uniaxial tension or bending tests on root segments. The transverse soil resistance can be estimated using models or by experiments such as penetrometer testing. Estimating realistic interface behaviour between real roots and soil might be more complicated. Roots might have root hairs and release exudate that strongly affects the soil in the vicinity of the root (the so-called "rhizophere"). Future work should focus on establishing realistic values for field soils and real plant roots.

The developed model is computationally friendly (typically the set of differential equations could be solved in under a second), yet maintains the key "ingredients" governing root-soil interaction and therefore mechanical root-reinforcement. This makes large parametric studies feasible, which can aid in identifying the relative influence of various parameters on root-reinforcement, such as root length, stiffness, strength, architecture, branching, angle between root, and shear plane. Thus, this model might aid in answering some of the long-standing questions in the root-reinforcement community. For example, a more detailed insight might be provided into quantifying (1) the effect of (sequential) mobilisation of root strength in direct shear based on shear deformation rather than using a FBM, (2) the effect of the angle between root and shear plane, (3) the effect or root bending and shear forces on root-reinforcement, or (4) the effect of root architecture/topology.

It should also be noted that the developed model could be used to efficiently and precisely define the equivalent continuum properties in hybrid beam element-finite element models such as that proposed by Liang et al.[15]

DATA STATEMENT

The Python code used to produce predictions for single roots in Experiment A is available online,[35] as is all data required to reproduce figures in this manuscript.[36]

NOMENCLATURE

- Δu relative axial soil-root displacement (mm)
- Δw relative transverse soil-root displacement (mm)
- δ soil-root interface friction angle (rad)
- ϵ_a axial root strain [-]
- γ' soil effective unit weight (Nmm^{-3})
- ζ_a fraction of mobilised ultimate axial soil-root resistance [-]
- ζ_l fraction of mobilised ultimate transverse soil-root resistance [-]
- Θ_0 angle of the non-deformed root with the vertical (rad)
- θ root angle in local $x - y$ coordinate system (rad)
- κ root curvature ($\mathrm{rad\,mm}^{-1}$)
- ξ_1 parameter in root stress-strain curve (MPa)
- ξ_2 parameter in root stress-strain curve [-]
- ξ_3 parameter in root stress-strain curve (MPa)
- σ_t root tensile strength (MPa)
- σ'_n normal effective stress (MPa)
- $\sigma'_{n,l}$ additional normal effective stress due to transverse soil-root resistance (MPa)
- σ'_v vertical effective stress (MPa)
- $\sigma'_{v,0}$ overburden pressure (MPa)

- τ current soil-root friction (MPa)
- τ_u ultimate soil-root friction (MPa)
- ϕ' soil angle of internal friction (rad)
- ϕ_{cv} critical state friction angle (rad)
- χ fraction of change in soil effective stress due to matric suction [-]
- A root cross-sectional area (mm^2)
- A_{sh} cross-sectional area of shear plane (mm^2)
- $\overline{A}_s$ empirical constant in p-y curve [-]
- b_a axial soil-root resistance mobilisation parameter (mm)
- b_l transverse soil-root resistance mobilisation parameter (mm)
- b_{sh} shear plane thickness parameter (mm)
- c_r additional soil "cohesion" due to root-reinforcement effects (MPa)
- d root/root analogue diameter (mm)
- E_t tensile stiffness (MPa)
- E_b bending stiffness (MPa)
- $F_{parallel}$ root-reinforcement force in the direction of the shear plane (N)
- $F_{perpendicular}$ root-reinforcement force perpendicular to the shear plane (N)
- F_r root-reinforcement force (N)
- I second moment of inertia (mm^4)
- K coefficient of lateral earth pressure [-]
- K_0 coefficient of lateral earth pressure at rest [-]
- K_a coefficient of active lateral earth pressure [-]
- K_p coefficient of passive lateral earth pressure [-]
- k' Wu/Waldron multiplication factor [-]
- k_{py}initial p-y stiffness parameter (MNm^{-3})
- M internal moment force (Nmm)
- N internal axial force (N)
- p current transverse soil resistance (per unit root length) (Nmm^{-1})
- p_u ultimate transverse soil resistance (per unit root length) (MPa)
- q_a axial soil-root resistance (per unit root length) (Nmm^{-1})
- q_l transverse soil-root resistance (per unit root length) (Nmm^{-1})
- RAR root area ratio ($mm^2\ mm^{-2}$)
- s local coordinate along the displaced root axis (mm)
- u axial root displacement (along x-axis) (mm)
- u_s axial soil displacement (along x-axis) (mm)
- u_{sh} soil shear displacement (mm)
- V internal shear force (N)
- w transverse root displacement (along y-axis) (mm)
- w_s transverse soil displacement (along y-axis) (mm)
- X soil depth (mm)
- X_{sh} shear plane depth (mm)
- x local coordinate aligned with nondisplaced root segment axis (mm)
- Y lateral coordinate (mm)
- y local coordinate perpendicular to nondisplaced root segment axis (mm)

ACKNOWLEDGEMENTS

This research was funded by EPSRC grant EP/M020355/1, which is a collaboration between the University of Dundee, the University of Southampton, the University of Aberdeen, Durham University, and The James Hutton Institute. The James Hutton Institute receives funding from the Scottish Government (Rural & Environmental Services & Analytical Services Division). The authors are grateful to S. B. Mickovski for access to original images from Mickovski et al,[23] part of EPSRC grant GR/S43962/01.

ORCID

Gerrit J. Meijer https://orcid.org/0000-0002-2815-5480

REFERENCES

1. Wu TH, McKinnell WP III, Swanston DN. Strength of tree roots and landslides on Prince of Wales Island, Alaska. *Can Geotech J*. 1979;16(1):19-33.
2. Schwarz M, Rist A, Cohen D, et al. Root reinforcement of soils under compression. *J Geophys Res: Earth Surface*. 2015;120(10):2103-2120.
3. Pollen N, Simon A. Estimating the mechanical effects of riparian vegetation on stream bank stability using a fiber bundle model. *Water Resour Res*. 2005;41(7):W07025.
4. Mao Z, Saint-Andre L, Genet M, et al. Engineering ecological protection against landslides in diverse mountain forests: choosing cohesion models. *Ecol Eng*. 2012;45:55-69.
5. Dupuy L, Fourcaud T, Stokes A. A numerical investigation into factors affecting the anchorage of roots in tension. *Eur J Soil Sci*. 2005;56(3):319-327.
6. Mickovski SB, Stokes A, van Beek R, Ghestem M, Fourcaud T. Simulation of direct shear tests on rooted and non-rooted soil using finite element analysis. *Ecol Eng*. 2011;37(10):1523-1532.
7. Michalowski RL, Çermák J. Triaxial compression of sand reinforced with fibers. *J Geotech Geoenviron Eng*. 2003;129(2):125-136.
8. Michalowski RL. Limit analysis with anisotropic fibre-reinforced soil. *Géotechnique*. 2008;58(6):489-501.
9. Muir Wood D, Diambra A, Ibraim E. Fibres and soils: a route towards modelling of root-soil systems. *Soils Found*. 2016;56(5):765-778.
10. Wu TH, McOmber RM, Erb RT, Beal PE. Study of soil–root interaction. *J Geotech Eng (ASCE)*. 1988;114(12):1351-1375.
11. Wu TH, Watson A. In situ shear tests of soil blocks with roots. *Can Geotech J*. 1998;35(4):579-590.
12. Wu TH. *Root Reinforcement: Analyses and Experiments*, Eco- and Ground Bio-Engineering: The Use of Vegetation to Improve Slope Stability, vol. 103. Dordrecht: Springer; 2007.
13. Wu TH. Root reinforcement of soil: review of analytical models, test results and applications to design. *Can Geotech J*. 2013;50(3):259-274.
14. Duckett NR. Development of improved predictive tools for mechanical soil root interaction. *Ph.D. Thesis*: University of Dundee; 2014.
15. Liang T, Knappett JA, Duckett N. Modelling the seismic performance of rooted slopes from individual root–soil interaction to global slope behaviour. *Géotechnique*. 2015;65(12):995-1009.
16. Reese LC, Van Impe WF. *Single Piles and Pile Groups Under Lateral Loading*. 2nd ed. Leiden, The Netherlands: CRC; 2011.
17. Randolph M, Gourvenec S. *Offshore Geotechnical Engineering*. New York, US: Spon; 2011.
18. American Petroleum Institute. Recommended practice for planning, design and constructing fixed offshore platforms – working stress design: API recommended practice 2a-wsd, 21st edition, December 2000. errata and supplement 1, December 2002. American Petroleum Institute; 2000.
19. Jones E, Oliphant T, Peterson P, et al. SciPy: Open source scientific tools for Python. http://www.scipy.org/. Online; accessed 20/11/2017; 2001.
20. Ekanayake JC, Marden M, Watson AJ, Rowan D. Tree roots and slope stability: a comparison between Pinus radiata and kanuka. *N Z J For Sci*; 27(2):216-233.
21. Fan C-C, Su C-F. Role of roots in the shear strength of root-reinforced soils with high moisture content. *Ecol Eng*. 2008;33(2):157-166.
22. Mickovski SB, Hallett PD, Bransby MF, Davies MCR, Sonnenberg R, Bengough AG. Mechanical reinforcement of soil by Willow roots: impacts of root properties and root failure mechanism. *Soil Sci Soc Am J*. 2009;73(4):1276-1285.
23. Mickovski SB, Bengough AG, Bransby MF, Davies MCR, Hallett PD, Sonnenberg R. Material stiffness, branching pattern and soil matric potential affect the pullout resistance of model root systems. *Eur J Soil Sci*. 2007;58(6):1471-1481.
24. Meijer GJ, Bengough AG, Knappett JA, et al. In situ root identification through blade penetrometer testing—part 1: interpretative models and laboratory testing. *Géotechnique*. 2017b;68(4):303-319. https://doi.org/10.1680/jgeot.16.P.203
25. Lauder K. The performance of pipeline ploughs. *Ph.D. Thesis*: University of Dundee; 2010.
26. Oda M, Iwashita K. *Mechanics of Granular Materials: An Introduction*. Rotterdam: Balkema; 1999.
27. Shewbridge SE, Sitar N. Deformation characteristics of reinforced sand in direct shear. *J Geotech Eng (ASCE)*. 1989;115(8):1134-1147.
28. Fredlund DG, Rahardjo H. *Soil Mechanics for Unsaturated Soils*. New York: John Wiley & Sons Inc.; 1993.
29. Lehane BM, White DJ. Lateral stress changes and shaft friction for model displacement piles in sand. *Can Geotech J*. 2005;42:1039-1052.
30. Meijer GJ, Bengough AG, Knappett JA, Loades KW, Nicoll BC. In situ root identification through blade penetrometer testing—part 2: field testing. *Géotechnique*. 2017a;68(4):320-331. https://doi.org/10.1680/jgeot.16.P.204
31. Meijer GJ, Bengough AG, Knappett JA, Loades KW, Nicoll BC. In situ measurement of root-reinforcement using the corkscrew extraction method. *Can Geotech J*. 2018;55(10):1372-1390. https://doi.org/10.1139/cgj-2017-0344
32. Giadrossich F, Schwarz M, Cohen D, Preti F, Or D. Mechanical interactions between neighbouring roots during pullout tests. *Plant Soil*. 2013;367(1–2):391-406.
33. Coppin N, Richards I. *Use of Vegetation In Civil Engineering, CIRIA Book 10*. Kent: Butterworths; 1990.
34. Bengough AG, Mullins CE. Mechanical impedance to root growth: a review of experimental techniques and root growth responses. *J Soil Sci*. 1990;41(3):341-358.

35. Meijer GJ. GJMeijer/RootBeam v1.0. https://doi.org/10.5281/zenodo.1465758; 2018.
36. Meijer GJ, Muir Wood D, Knappett JA, Bengough AG, Liang T. Analysis of coupled axial and lateral deformation of roots in soil—figure data. https://doi.org/10.15132/10000137; 2018.

How to cite this article: Meijer GJ, Muir Wood D, Knappett JA, Bengough GA, Liang T. Analysis of coupled axial and lateral deformation of roots in soil. *Int J Numer Anal Methods Geomech*. 2018;1–24. https://doi.org/10.1002/nag.2880

APPENDIX: DERIVATION OF DIFFERENTIAL EQUATIONS

Consider a small element with length ds along the root. The root has a diameter d, bending and tensile stiffness E_b and E_t, a cross-sectional area A, and a second moment of inertia I.

It is assumed that the axial and transverse resistance act along a straight line connecting the beginning and end point of the small element ds; see Figure A1. q_a acts parallel to this line, while q_l acts perpendicularly. The (small) effect the root curvature has on the equilibrium of forces is therefore ignored.

There has to be equilibrium of forces in all three degrees of freedom. Considering equilibrium in the direction of ds:

$$(N+\mathrm{d}N)\cos\left(\frac{1}{2}\mathrm{d}\theta\right)-(V+\mathrm{d}V)\sin\left(\frac{1}{2}\mathrm{d}\theta\right)-N\cos\left(\frac{1}{2}\mathrm{d}\theta\right)-V\sin\left(\frac{1}{2}\mathrm{d}\theta\right)=-q_a\mathrm{d}s. \tag{A1}$$

Equilibrium in the direction perpendicular to ds:

$$(V+\mathrm{d}V)\cos\left(\frac{1}{2}\mathrm{d}\theta\right)+(N+\mathrm{d}N)\sin\left(\frac{1}{2}\mathrm{d}\theta\right)-V\cos\left(\frac{1}{2}\mathrm{d}\theta\right)+N\sin\left(\frac{1}{2}\mathrm{d}\theta\right)=-q_l\mathrm{d}s. \tag{A2}$$

And for equilibrium for the rotational degree of freedom (considering moment equilibrium along the right end of segment ds):

$$\mathrm{d}M=-\frac{1}{2}q_l\mathrm{d}s^2-N\sin\left(\frac{1}{2}\mathrm{d}\theta\right)\mathrm{d}s+V\cos\left(\frac{1}{2}\mathrm{d}\theta\right)\mathrm{d}s. \tag{A3}$$

The incremental rotation (dθ) is considered small, therefore,

$$\cos\left(\frac{1}{2}\mathrm{d}\theta\right)\approx 1, \tag{A4}$$

$$\sin\left(\frac{1}{2}\mathrm{d}\theta\right)\approx\tan\left(\frac{1}{2}\mathrm{d}\theta\right)\approx\frac{1}{2}\mathrm{d}\theta. \tag{A5}$$

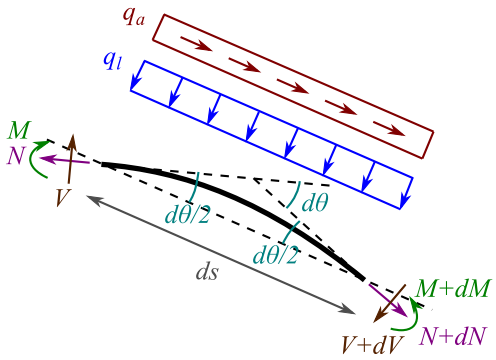

FIGURE A1 Equilibrium of a small element ds along the displaced root axis [Colour figure can be viewed at wileyonlinelibrary.com]

Now the equilibrium conditions in all degrees of freedom can be simplified to

$$-q_a \mathrm{d}s = \mathrm{d}N - V\mathrm{d}\theta - \frac{1}{2}\mathrm{d}V\mathrm{d}\theta, \tag{A6}$$

$$-q_l \mathrm{d}s = \mathrm{d}V + N\mathrm{d}\theta + \frac{1}{2}\mathrm{d}N\mathrm{d}\theta, \tag{A7}$$

$$\mathrm{d}M = -\frac{1}{2}q_l \mathrm{d}s^2 - \frac{1}{2}N\mathrm{d}\theta\mathrm{d}s + V\mathrm{d}s. \tag{A8}$$

Dropping second order terms and differentiating to ds yields

$$-q_a = \frac{\mathrm{d}N}{\mathrm{d}s} - V\frac{\mathrm{d}\theta}{\mathrm{d}s}, \tag{A9}$$

$$-q_l = \frac{\mathrm{d}V}{\mathrm{d}s} + N\frac{\mathrm{d}\theta}{\mathrm{d}s}, \tag{A10}$$

$$\frac{\mathrm{d}M}{\mathrm{d}s} = V. \tag{A11}$$

The moment M in the beam depends on the curvature κ. The exact curvature is equal to change in beam angle θ along axis s. This is also valid for large deformations. Therefore,

$$\kappa = \frac{\mathrm{d}\theta}{\mathrm{d}s}, \tag{A12}$$

$$M = -E_b I\kappa = -E_b I\frac{\mathrm{d}\theta}{\mathrm{d}s}. \tag{A13}$$

Differentiating Equation A13 twice with respect to s and Equation A11 once with respect to s gives two separate expressions for $\mathrm{d}^2M/\mathrm{d}s^2$:

$$\frac{d^2M}{ds^2} = -E_b I\frac{\mathrm{d}^3\theta}{\mathrm{d}s^3} = \frac{\mathrm{d}V}{\mathrm{d}s}. \tag{A14}$$

Substituting $\mathrm{d}V/\mathrm{d}s$ from Equation A10 into Equation A14 yields the first of the differential equations describing the displacements of the deformed root:

$$E_b I\frac{\mathrm{d}^3\theta}{\mathrm{d}s^3} = q_l + N\frac{\mathrm{d}\theta}{\mathrm{d}s}. \tag{A15}$$

A second differential equation, describing the axial force N along s, follows from differentiating Equation A13 to find V using Equation A11 and subsequently substituting the resulting expression for V in Equation A9:

$$\frac{\mathrm{d}N}{\mathrm{d}s} = -q_a - E_b I\frac{\mathrm{d}^2\theta}{\mathrm{d}s^2}\frac{\mathrm{d}\theta}{\mathrm{d}s}. \tag{A16}$$

The axial force can be calculated from the axial strain ϵ_a:

$$N = E_t A\epsilon_a. \tag{A17}$$